

# Multi-temporal SAR image decomposition into strong scatterers, background, and speckle

Sylvain Lobry, Loïc Denis, Florence Tupin

**Abstract**—Speckle phenomenon in synthetic aperture radar (SAR) images makes their visual and automatic interpretation a difficult task. To reduce strong fluctuations due to speckle, total variation (TV) regularization has been proposed by several authors to smooth out noise without blurring edges. A specificity of SAR images is the presence of strong scatterers having a radiometry several orders of magnitude larger than their surrounding region. These scatterers, especially present in urban areas, limit the effectiveness of TV regularization as they break the assumption of an image made of regions of constant radiometry. To overcome this limitation, we propose in this paper an image decomposition approach.

There exists numerous methods to decompose an image into several components, notably to separate textural and geometrical information. These decomposition models are generally recast as energy minimization problems involving a different penalty term for each of the components. In this framework, we propose an energy suitable for the decomposition of SAR images into speckle, a smooth background and strong scatterers, and discuss its minimization using max-flow/min-cut algorithms. We make the connection between the minimization problem considered, involving the L0 pseudo-norm, and the generalized likelihood ratio test used in detection theory. The proposed decomposition jointly performs the detection of strong scatterers and the estimation of the background radiometry.

Given the increasing availability of time series of SAR images, we consider the decomposition of a whole time series. New change detection methods can be based on the temporal analysis of the components obtained from our decomposition.

**Index Terms**—SAR, Image decomposition, TV, L0, Change detection.

## I. INTRODUCTION

Due to the coherent nature of SAR imaging technique, SAR images suffer from strong fluctuations related to the speckle phenomenon. While containing information about the sub-resolution texture of the scene, speckle is often regarded as undesirable noise for image interpretation tasks. Speckle is then typically modeled as a multiplicative noise.

While image denoising and restoration are among the oldest challenges addressed in image processing, most algorithms developed in the field of image processing are designed to deal with an additive Gaussian noise and are thus not directly applicable to SAR images.

S. Lobry is with LTCI, CNRS, Télécom ParisTech, Université Paris-Saclay, 75013, Paris, France and the Centre National d'Études Spatiales (CNES), Toulouse, France, e-mail: sylvain.lobry@telecom-paristech.fr.

L. Denis is with the Laboratoire Hubert Curien, UMR 5516 CNRS, Université de Saint-Etienne and Télécom Saint-Etienne, Saint-Etienne, France, e-mail: loic.denis@univ-st-etienne.fr.

F. Tupin is with LTCI, CNRS, Télécom ParisTech, Université Paris-Saclay, 75013, Paris, France, e-mail: florence.tupin@telecom-paristech.fr

Manuscript received FIXME; revised FIXME.

The simplest way to reduce speckle fluctuations is spatial multi-looking which amounts to averaging pixel values within a sliding window. This speckle variance reduction is obtained at the cost of a resolution loss proportional to the size of the averaging window. While it may produce satisfying results in homogeneous areas, it strongly blurs textured areas, edges between regions and bright scatterers.

Numerous approaches have been proposed to prevent the introduction of blur by mixing values from distinct regions. Lee *et al.* [1] locally select the best window among a few oriented windows. The IDAN algorithm [2] builds an adaptive window by region growing. Several methods have been derived from the non-local means (NL-means) approach by Buades *et al.* [3]. These methods select similar pixels in an extended window based on patch-similarity [4]–[10]. Another family of methods reduce speckle by regularization, i.e., by computing the maximum a posteriori estimate under a given prior. Wavelet-based approaches model the distribution of wavelet coefficients [11]–[13]. Total variation (TV) regularization penalizes variations between neighboring pixels while preserving sharp edges [14]. Total variation has been applied to the regularization of SAR amplitudes [15]–[17], SAR intensities [18], [19] and log-transformed intensities [20] using different optimization strategies (discrete optimization by graph-cuts, gradient descent, Douglas-Rachford splitting or the alternating directions method of multipliers). We refer the reader to the two recent review papers [21] and [22] for an in-depth analysis of speckle reduction methods.

Man-made structures such as buildings, fences or transmission towers produce very strong back-scattering, with intensities much larger than the surrounding area. Such scatterers are especially numerous in urban areas. Isolated strong scatterers are challenging for speckle reduction methods because they generally break the statistical assumptions made about the radar scene: repetition of similar patches within the search window (patch-based methods), sparse representation in the wavelets domain (wavelets-based methods), or piece-wise constant regions (TV minimization). It is then necessary to identify and process these points separately to prevent from spreading these large values. Strong scatterers can be detected using likelihood ratio tests [23], [24]. These detectors compare the values in the center of a window with the rest of the window, considered as purely background. In dense urban areas, the presence of other point-like scatterers in the vicinity strongly deteriorates the performance. It is thus necessary to perform jointly the detection of strong scatterers with the estimation of the background radiometry. The decomposition method that we propose in the present paper achieves such a

joint detection of point-like scatterers and estimation of the background. It applies to multi-temporal stacks of images by detecting scatterers at each date, even if they are not present at other dates due to some change occurring.

This paper extends the decomposition models presented in [25], [26] in the following ways: We derive the decomposition model from a connection between scatterers detection and maximum a posteriori estimation with a regularization term based on L0 pseudo-norm (section II). The proposed decomposition model can provide a multi-temporal image of detected scatterers and a smoothly varying multi-temporal background image, or a simpler decomposition into multi-temporal scatterers image and a time-invariant background. Computing the decomposition requires solving a challenging large-scale combinatorial problem. We describe two algorithmic approaches (section III): an exact discrete optimization based on finding the minimum cut in a large 4-D graph, and a faster but approximate method based on block processing with overlaps. We show on numerical experiments that the choice of the L0 non-convex penalty significantly improves the detection of scatterers compared to the usual L1 norm surrogate (section IV). We illustrate how the detected scatterers can be used in a subsequent processing step for change detection purposes (section V).

## II. SPARSE + SMOOTH DECOMPOSITION MODEL FOR MULTI-TEMPORAL DATA

### A. From detection to estimation under L0 prior

Let us consider first the problem of detecting strong scatterers in a speckled region of given radiometry  $u_B$ . At each pixel  $i$ , the detection problem amounts to deciding between two hypotheses: the absence ( $\mathcal{H}_0$ ) or presence ( $\mathcal{H}_1$ ) of a strong scatterer in addition to the other scatterers that form the background:

$$\begin{cases} \mathcal{H}_0 : & u_{S_i} = 0 \\ \mathcal{H}_1 : & u_{S_i} > 0, \end{cases} \quad (1)$$

where  $u_{S_i}$  is the radiometry of the additional scatterer.

Under the assumption of uncorrelated speckle and point-like scatterers, this hypothesis test can be performed independently at each pixel by studying the likelihood ratio:

$$\log \frac{\mathbb{P}(v_i|u_{B_i} + u_{S_i})}{\mathbb{P}(v_i|u_{B_i})} \stackrel{\mathcal{H}_1}{\underset{\mathcal{H}_0}{\geq}} \lambda, \quad (2)$$

with  $v_i$  the observed amplitude at pixel  $i$  (i.e., speckle-corrupted) and  $\lambda$  a threshold. This likelihood ratio test can not be readily applied since the radiometry  $u_{S_i}$  is unknown. Replacing  $u_{S_i}$  by the maximum likelihood estimate leads to the generalized likelihood ratio test (GLRT) [27]:

$$\arg \max_{u_{S_i} \geq 0} \log \mathbb{P}(v_i|u_{B_i} + u_{S_i}) \stackrel{\mathcal{H}_1}{\underset{\mathcal{H}_0}{\geq}} \lambda + \log(\mathbb{P}(v_i|u_{B_i})). \quad (3)$$

In words, the presence of an additional scatterer is detected at pixel  $i$  if the log-likelihood of the observed amplitude  $v_i$  is improved at least by  $\lambda$  when hypothesizing that a scatterer is present in addition to the background scatterers. The threshold  $\lambda$  sets the false alarm rate: increasing  $\lambda$  reduces the probability

of wrongly selecting hypothesis  $\mathcal{H}_1$  under  $\mathcal{H}_0$ , at the cost of reducing the detection probability.

This detection problem can be stated as an estimation problem, i.e., as the estimation of the radiometry of the additional scatterer  $u_{S_i}$ , where a zero estimated radiometry corresponds to the absence of the additional scatterer at pixel  $i$ :

$$\widehat{u_{S_i}} = \arg \min_{u_{S_i} \geq 0} [-\log \mathbb{P}(v_i|u_{B_i} + u_{S_i}) + \lambda \cdot (u_{S_i} \neq 0)], \quad (4)$$

where the notation  $\lambda \cdot (u_S \neq 0)$  refers to value  $\lambda$  whenever  $u_S \neq 0$ , and 0 when  $u_S = 0$ . Equation (4) is completely equivalent to equation (3), and can be extended to a whole image. The estimation of the vector of all radiometries  $\mathbf{u}_S$ , for a given vector of corresponding background radiometries  $\mathbf{u}_B$  and under our pixel-independence assumption, is given by:

$$\widehat{\mathbf{u}_S} = \arg \min_{\mathbf{u}_S \geq 0} [-\sum_i \log \mathbb{P}(v_i|u_{B_i} + u_{S_i}) + \lambda \|\mathbf{u}_S\|_0], \quad (5)$$

where the positivity constraint  $\mathbf{u}_S \geq 0$  applies component-wise and the L0 pseudo-norm corresponds to the number of non-zero components of vector  $\mathbf{u}_S$ .

### B. Joint estimation of the background and of strong scatterers

Direct applicability of the estimation formulation given in equation (5) is limited because it requires the knowledge of the background radiometry  $\mathbf{u}_B$ . Estimation of this background radiometry requires to exclude strong scatterers, i.e., the detection of all scatterers in  $\mathbf{u}_S$ . The two components  $\mathbf{u}_B$  and  $\mathbf{u}_S$  must thus be jointly estimated:

$$(\widehat{\mathbf{u}_S}, \widehat{\mathbf{u}_B}) = \arg \min_{\mathbf{u}_S \geq 0, \mathbf{u}_B \geq 0} [-\sum_i \log \mathbb{P}(v_i|u_{B_i} + u_{S_i}) + \lambda \|\mathbf{u}_S\|_0 + \psi(\mathbf{u}_B)], \quad (6)$$

where  $\psi$  is a smoothness term necessary to enforce the regularity of the background and thus prevent problem degeneracy<sup>1</sup>. Regularization term  $\psi$  introduces a coupling between all unknowns, i.e., the minimization problem in (6) is not separable. With the L0 term, the optimization problem is combinatorial (non-convex and discontinuous). Given the large scale of the problem (typically millions to billions of unknown pixel radiometries to estimate), two approaches can be considered:

- **convex relaxation:** the L0 term is generally replaced by the L1 norm to turn the combinatorial minimization problem into a convex minimization problem;
- **combinatorial optimization:** direct minimization of (6) is possible for some specific choices of the regularization term  $\psi$ .

The first approach suffers from two drawbacks: (i) under speckle noise, the neg-log-likelihood is non-convex, which prevents direct application of standard convex optimization methods; (ii) with the L1 norm, the estimation problem is no longer equivalent to the detection problem. We show in

<sup>1</sup>in the absence of the smoothness term  $\psi$ , the decomposition is trivial:  $\widehat{\mathbf{u}_S} = \mathbf{0}$  and  $\widehat{\mathbf{u}_B} = \widehat{\mathbf{u}_B}^{(ML)} \equiv \arg \min_{\mathbf{u}_B \geq 0} -\sum_i \log \mathbb{P}(v_i|u_{B_i})$  is the maximum likelihood estimate of the background.

section IV that this leads to a non-constant false alarm rate: scatterers are mainly detected in darker areas.

The second approach consists of applying a combinatorial optimization method to the problem, for a given discretization of the radiometries. It restates the original optimization problem as a minimum cut / maximum flow search on a graph [28]. It applies to discrete optimization problems involving (possibly non-convex) separable terms and convex pairwise terms, and is well suited (i.e., the graph is sparsest) for anisotropic total variation:

$$TV(\mathbf{u}) = \sum_{i \sim j} w_{i,j} |u_i - u_j|, \quad (7)$$

where  $i \sim j$  indicates that  $i$  and  $j$  are indices of two neighboring pixels, and  $w_{i,j}$  are weights. In the simplest form, only the 4 nearest neighbors are considered and all weights  $w_{i,j}$  are equal to 1. To reduce the metrication effects, farther neighbors can also be considered, with smaller weights, see for example [29]. In the following, we will consider a smoothness term  $\psi$  based on total variation (7) so that a graph-cut method can be applied to solve the non-convex minimization problem.

### C. Multi-temporal decomposition model

We consider the decomposition of a time series of SAR images into 3 components: a spatio-temporal background, additional point-like scatterers, and speckle noise. A multi-temporal stack, represented by a vector  $\mathbf{v}$ , is decomposed by jointly estimating the background  $\mathbf{u}_B$  and the additional scatterers  $\mathbf{u}_S$ . The speckle component  $\mathbf{n}$  then corresponds to the ratio between observed amplitudes and the estimated radiometries, according to the multiplicative speckle model:

$$\mathbf{v} = (\mathbf{u}_B + \mathbf{u}_S) \times \mathbf{n}, \quad (8)$$

where the multiplication is applied component-wise.

Under Goodman's fully developed speckle model [30], the observed amplitude  $v_{t,i}$  at pixel  $i$  and time  $t$  follows a Rayleigh distribution:

$$p(v_{t,i}|u_{t,i}) = \frac{2v_{t,i}}{u_{t,i}^2} \exp\left(-\frac{v_{t,i}^2}{u_{t,i}^2}\right), \quad (9)$$

where  $u_{t,i} = u_{Bt,i} + u_{St,i}$  is the radiometry at pixel  $i$  and time  $t$ . Other statistical distributions may be considered, for example Rice distribution which is more accurate when one strong scatterer is dominant in the resolution cell ( $u_{St,i} \gg u_{Bt,i}$ ). Note that with the choice of Rayleigh distribution, the generalized likelihood ratio test (3) takes the form:

$$\frac{v_i^2}{u_B^2} - \log \frac{v_i^2}{u_B^2} \frac{\mathcal{H}_1}{\mathcal{H}_0} \geq \lambda + 1. \quad (10)$$

Since the test depends only on the ratio  $v_i/u_B$  which is Rayleigh distributed with parameter 1 under  $\mathcal{H}_0$ , the threshold  $\lambda$  sets a constant false alarm rate (i.e.,  $\lambda$  need not be tuned with the level  $u_B$ ).

To apply the joint estimation of the background and detection of scatterers described in the preceding sections, the regularization term  $\psi(\mathbf{u}_B)$  needs to be set. Apart from the presence of many strong-scatterers, SAR images can reasonably well

be described by smooth regions (with few variations of the radiometry) separated by sharp edges. In a time series, changes with time are rather smooth (e.g., vegetation changes) and pixels within a region of homogeneous radiometry generally keep comparable radiometries. When an abrupt change occurs, it is important to prevent from smoothing in time its apparition. We consider using a spatio-temporal total variation to impose some spatial and temporal smoothing while preserving sharp edges / changes. The proposed spatio-temporal regularization is:

$$TV_{3D}^\alpha(\mathbf{u}_B) = \sum_t \sum_{i \sim j} w_{i,j} |u_{Bt,i} - u_{Bt,j}| + \alpha \sum_i \sum_t |u_{Bt+1,i} - u_{Bt,i}|, \quad (11)$$

where  $\alpha$  is the weight along the temporal direction.

If  $\alpha$  is set to a very large value, no temporal change is possible and a constant (in time) background component is estimated. We denote  $TV_{3D}^\infty$  the regularization in this simplified case of a time-invariant background.

With Rayleigh likelihood and the  $TV_{3D}$  regularization, the joint decomposition amounts to solving the following minimization problem:

$$\arg \min_{\mathbf{u}_S \geq 0, \mathbf{u}_B \geq 0} \sum_{i,t} \left[ 2 \log(u_{Bt,i} + u_{St,i}) + \frac{v_{t,i}^2}{(u_{Bt,i} + u_{St,i})^2} \right] + \lambda \|\mathbf{u}_S\|_0 + \beta TV_{3D}^\alpha(\mathbf{u}_B). \quad (12)$$

## III. OPTIMIZATION USING GRAPH-CUTS

### A. Exact discrete optimization

To apply the graph-cuts combinatorial optimization method to the minimization problem defined in equation (12), we need that it be formulated as:

$$\arg \min_{\mathbf{x}} \sum_{t,i} f_0(x_{i,t}) + \sum_{(i,t) \sim (i',t')} f_1(x_{i,t}, x_{i',t'}), \quad (13)$$

i.e., as the sum of separable terms  $f_0$  and pairwise terms  $f_1$  involving (spatio-temporal) neighbors  $(i,t)$  and  $(i',t')$ .

For any fixed background  $\mathbf{u}_B$ , the equivalence between the estimation formulation (4) and the detection formulation (3) shows that the computation of the optimal vector of scatterers  $\mathbf{u}_S^*$  is readily obtained by simple testing against a threshold, for each pixel. It follows from (10) that the optimal  $\mathbf{u}_S$  is given by:

$$u_{St,i}^*(u_{Bt,i}) = \begin{cases} v_{t,i} - u_{Bt,i} & \text{if } v_{t,i} > u_{Bt,i} \\ & \text{and } \frac{v_i^2}{u_B^2} - \log \frac{v_i^2}{u_B^2} \geq \lambda + 1, \\ 0 & \text{otherwise.} \end{cases} \quad (14)$$

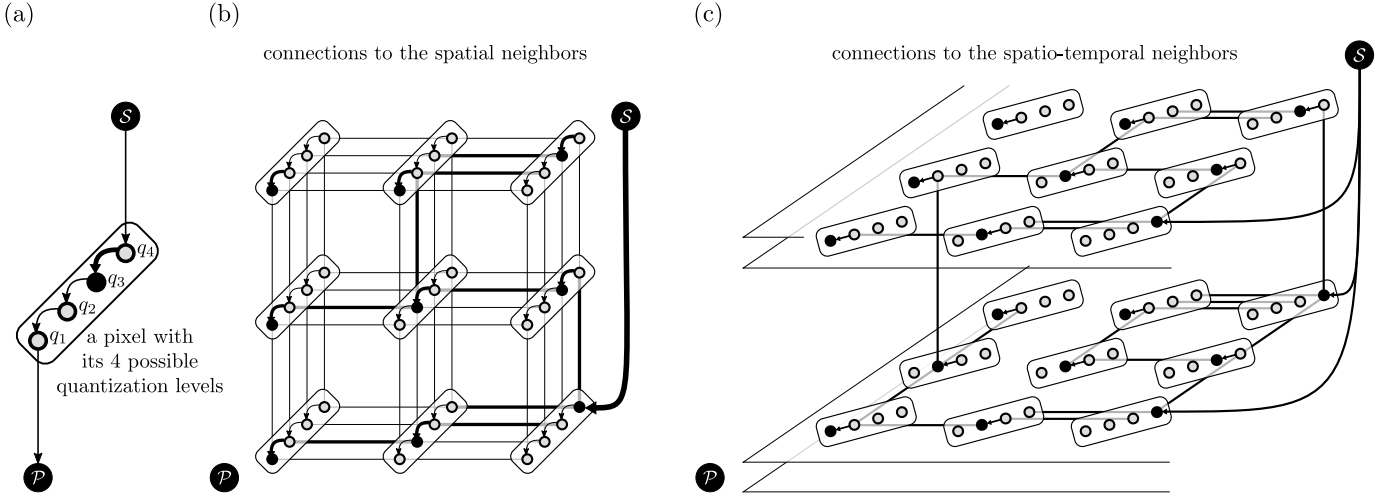


Fig. 1. Graph construction used to solve the image decomposition minimization problem. (a) A set of  $q_{max}$  nodes (one for each quantization level) is created for each pixel of the multi-temporal image  $\mathbf{u}_B$ . Edges directed downstream are created, from the source  $S$  to the sink  $\mathcal{P}$ . The edge in the minimum cut, shown with a thick line, indicates that the quantization level right below (colored in black) is the optimal value. (b) Bi-directional edges are added between corresponding quantization levels for all pairs of spatially adjacent pixels (edges from the source and to the sink that are not in the minimum cut are omitted in the drawing). (c) Bi-directional edges are also added between temporal neighbors. Only edges in the minimum cut are shown here, with the corresponding optimal level at each pixel denoted by a black disk.

By substituting  $\mathbf{u}_S$  with its optimal value  $\mathbf{u}_S^*(\mathbf{u}_B)$  in the minimization problem (12), we get the sought formulation of equation (13), with

$$\mathbf{x} = \mathbf{u}_B \quad (15)$$

$$f_0(x_{i,t}) = 2 \log(u_{Bt,i} + u_{S^*,i}(u_{Bt,i})) + \frac{v_{t,i}^2}{(u_{Bt,i} + u_{S^*,i}(u_{Bt,i}))^2} + \lambda \cdot (u_{S^*,i}(u_{Bt,i}) \neq 0) \quad (16)$$

$$f_1(x_{i,t}, x_{j,t}) = \beta \cdot w_{i,j} \cdot |u_{Bt,i} - u_{Bt,j}| \quad (17)$$

$$f_1(x_{i,t}, x_{i,t+1}) = \beta \cdot \alpha \cdot |u_{Bt+1,i} - u_{Bt,i}|. \quad (18)$$

We apply the graph construction method of Ishikawa [28] to restate the minimization problem as the search of a minimum cut in a graph. We choose a (not necessarily uniform) quantization of values of the background:  $\{q_1, q_2, \dots, q_{max}\}$ . We then create a set of nodes representing all quantization levels for each (spatio-temporal) pixel, see Fig. 1(a). Oriented edges are created from the source to the nodes associated with level  $q_{max}$ , then within a set of nodes associated to a given pixel, each node is connected to its preceding quantization level. Finally, the nodes representing level  $q_1$  are connected to the sink. The capacity of the edge pointing to the node associated with pixel  $(i, t)$  and quantization level  $q_c$  is set to  $f_0(q_c)$ . Upstream edges with infinite capacity are also created to enforce that a minimum cut separates the source and the sink at a unique level for each pixel.

Spatial neighbors are then connected with bi-directional edges: two nodes representing the same quantization level  $q_c$  are connected and the capacity of the edge is set to  $\beta \cdot w_{i,j} \cdot (q_{c+1} - q_c)$ . Finally, temporal neighbors are connected by creating bi-directional edges between nodes representing the same quantization level  $q_c$ , with a capacity set to  $\alpha \cdot \beta$ .

In figure 2, we show the first and the last images obtained by applying the proposed decomposition on a SAR time series

from Saint-Gervais (France) acquired by TerraSAR-X satellite.

**Computational and memory complexity:** The graph construction requires a large amount of memory that limits its application to small regions of interest and/or short time series. The number of vertices is proportional to the number of images in the time series, the number of pixels of each image, and the number of quantization levels. The number of edges is proportional to the number of nodes (about 8 times the number of nodes). We used the graph-cuts implementation described in [31]. In this graph implementation, each vertex requires 48 bytes of storage, and each edge requires 32 bytes. Hence, the memory footprint of the graph representation limits the size of the series of images that can be processed. For example, a series of 20 images of size  $300 \times 400$  with a quantification into 50 levels requires 33.7GiB of RAM for the graph construction. However, when  $\psi = TV_{3D}^\infty$ , the problem only involves one background. Solving the same problem with this regularization only requires 1.35GiB, simplifying the exact optimization of the proposed model.

Regarding the computational cost, the worst-case complexity of the minimum cut is  $O(EV^2|C|)$  where  $C$  is the value of the minimum cut,  $E$  is the number of edges and  $V$  the number of vertices. In practice, the experimental complexity scales almost linearly with the number of nodes [31]. On a computer with an Intel® Xeon(R) CPU E5-1620 with 16Gb of RAM, the algorithm takes 52,04s to compute a decomposition on 2 images of  $300 \times 400$  pixels with 50 levels of quantification. Note that we do not fully benefit from the power of the processor as the implementation of the algorithm used is single-core. Algorithms computing the grid-cut in parallel have also been proposed (see [32]) and more compact memory representations that exploit the regularity of the graph have been introduced in [33].

To reduce the computational and memory complexity, a

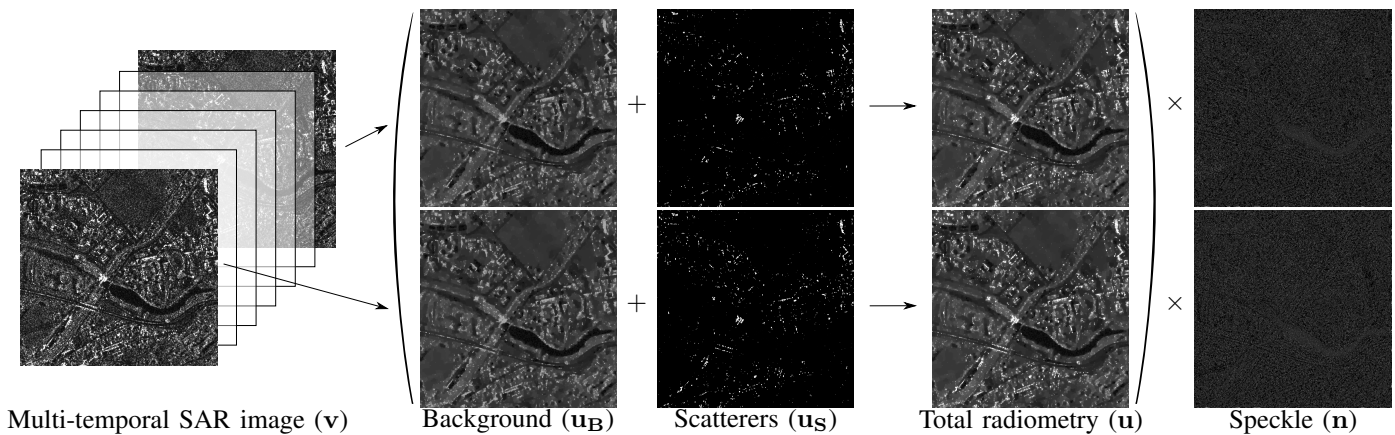


Fig. 2. Decomposition of a time series of TerraSAR-X images of Saint-Gervais, France. Only the first and the last image of the decomposition are shown.

subset of all quantization levels can be considered at a time to get an approximate solution, see [34], [35]. We describe in section III-B another approach based on block processing to further reduce memory requirements.

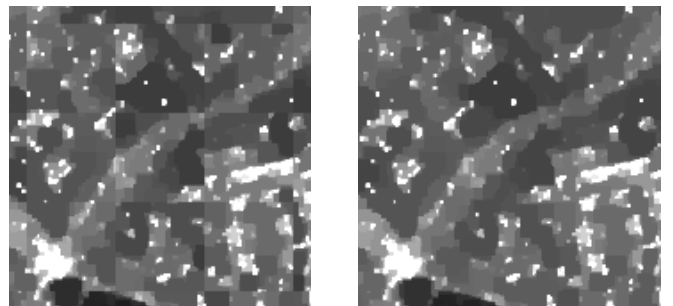
**Quantization of the radiometry:** The selection of the quantization levels used to represent the background radiometries  $\mathbf{u}_B$  requires to find a trade-off between accuracy (the more quantization levels the better) and the memory complexity (the graph footprint is proportional to the number of quantization levels). We used an adaptive method to set the quantization levels. We manually select the proportion  $p$  of the image considered to be in the background (a typical value is around 95%, but may be adapted according to the density of scatterers). The quantization levels are then computed from the quantiles of the  $p$  lowest observed values of the first image. Note that only the background values  $\mathbf{u}_B$  need to be quantified, the bright scatterers component  $\mathbf{u}_S$  with the highest dynamic range is not quantified (see equation 14).

### B. Memory efficient optimization

To apply the method to large images and/or long time series, it is necessary to develop a method for limited-memory graph-cut optimization.

*a) Method:* Memory usage of the graph-cut method is proportional to the number of pixels in the series. The required memory can thus be reduced by computing the optimization locally, on spatio-temporal blocks extracted from the time series. Even though our model involves only second order cliques, limiting the direct interactions to the immediate neighborhood, the maximum a posteriori estimate involves long-range correlations, i.e., during the optimization, regularization effects are propagated over long distances. Simple division of the image into smaller blocks thus results into visible *block artifacts*, as can be observed in figure 3a. These *block artifacts* are due to the lack of context: a constant area in the global optimum that gets divided into two regions during the block-processing is represented by two different (constant) values with an artificial discontinuity between the blocks.

To introduce context in the window  $F$  of interest, it is necessary to perform the optimization on a bigger window  $C$



(a) Solution obtained by local optimization (computation window of size  $50^2$  leading to a block effect) (b) Exact solution obtained using the presented algorithm for a computation window of size  $150^2$

Fig. 3. Crops of the background component of the first image of the Saint-Gervais set obtained with the presented method (filling window of size  $50^2$ ).

containing all the objects partially presents in  $F$ . The proposed method works as follows:

- 1) To process a given window  $F$  (named filling window in the following), extract a larger computation window  $C$  such that  $F \subset C$ .
- 2) Perform the optimization using the graph-cuts method described in section III-A on the spatio-temporal window  $C$ .
- 3) Keep the results of the decomposition only in the (smaller) filling window  $F$ .
- 4) Slide the filling window  $F$  and repeat from step 1 until all the image has been covered by the filling window.

*b) Results:* We show in figure 4 the root mean squared error obtained by the block-processing approach for different sizes of the computation window (the size of the block  $F$  is kept constant and equal to  $50 \times 50$  pixels for this single-date image). The required memory grows quadratically with the spatial window size. It can be observed that on this image, the exact solution is obtained for computation windows  $C$  larger or equal to  $150 \times 150$  pixels (which requires only 8.6% of the amount of memory needed to process the whole image at once). When the computation window  $F$  is strictly smaller than the image size, the solution computed on the block  $F$  is

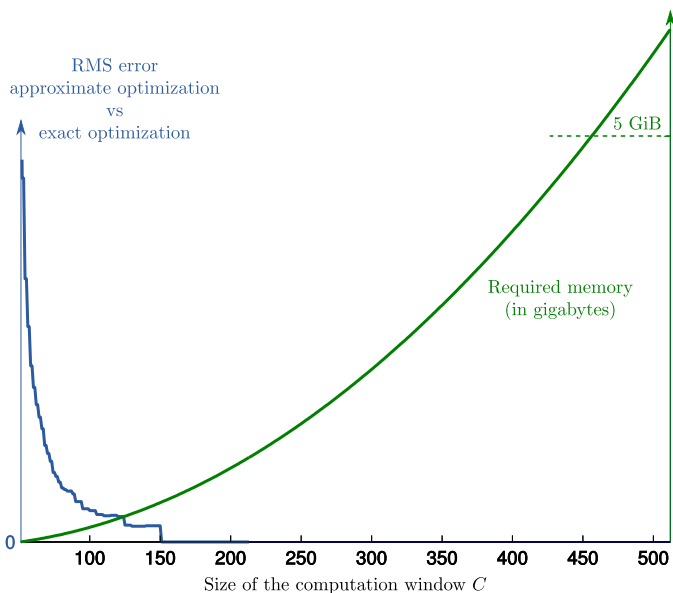


Fig. 4. Root mean squared error (RMSE) and memory used as a function of the size of the spatial computation window  $C$ , for the first image of the Saint-Gervais dataset.

not guaranteed to match the solution obtained from the whole image, i.e., it is only approximate.

#### IV. ADVANTAGE OF THE L0 PSEUDO-NORM OVER THE L1 RELAXATION

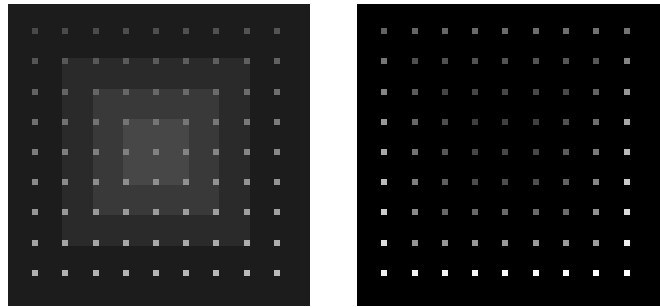
The combinatorial optimization method described in section III is applicable to the L0 pseudo-norm and to the L1 norm, and provides in both cases the global optimum. It is thus possible to compare the performance of the two formulations: the L0 penalty derived from the GLRT and the L1 norm widely used to obtain a convex relaxation of the minimization problem, see for example [36].

We either consider the original minimization problem as stated in equation (12), or a modified minimization problem where the L0 pseudo-norm is replaced by the L1 norm. When considering the modified minimization problem involving the L1 norm, the optimal  $\mathbf{u}_S$  is no longer given by a simple expression as in equation (14). Optimal values  $u_{S,i}^*$  are either zero, or if strictly positive, they must cancel the first partial derivative of the sum of the log-likelihood and the L1 norm, given below:

$$\frac{\partial}{\partial u_S} \left[ 2 \log(u_S + u_B) + \frac{v^2}{(u_S + u_B)^2} + \lambda u_S \right] = -\frac{2v^2}{(u_S + u_B)^3} + \frac{2}{u_S + u_B} + \lambda. \quad (19)$$

The only positive and real-valued root, as obtained by finding the roots of a third degree polynomial using a computer algebra system, is:

$$u_S^*(u_B) = t^{1/3} + \frac{4}{9\lambda^2 t^{1/3}} - \frac{3\lambda u_B + 2}{3\lambda}, \quad (20)$$



(a) Input noise-free image (b) Contrast (values up to 6.55)

Fig. 5. Input image used to compare L0 and L1 models.

with

$$t = \frac{v\sqrt{27\lambda^2 v^2 - 16}}{3^{3/2}\lambda^2} + \frac{27\lambda^2 v^2 - 8}{27\lambda^3}. \quad (21)$$

We consider a numerical experiment to compare the detection performance of L0 and L1 formulations, for various contrasts between point-like scatterers and a piece-wise constant background, see figure 5a. The contrast between each scatterer and the background is given in figure 5b. 100 noisy versions are then generated using a Rayleigh multiplicative model. The L0 and L1 models are applied to each of these images with a fixed value of  $\beta$  (set to 0.05) and various  $\lambda$  values.

The receiver operating characteristic (ROC) curves are drawn on figure 6 and compared with the ROC curve obtained using the method based on a local estimation of the background proposed in [24]. The L0 model outperforms both the L1 model and the detection based on local background estimation. We show in figure 7 the scatterers detected by each model, for an identical proportion of correct detections. The L0 model gives a uniform performance (correct detections and false detections are well distributed in the image), while the L1 model fails to detect scatterers in the regions with higher background radiometry and gives more false detections in low-radiometry areas. This phenomenon is confirmed by representing the evolution of the probability of false alarm (Pfa) and the probability of detection (Pd) as a function of the background radiometry, figure 8. The L0 term produces constant Pfa and Pd (note that, in the numerical simulation, when the background radiometry changes, the scatterer radiometry is adapted so as to keep a constant contrast:  $u_S = 40\% u_B$ ). In contrast, the Pfa and Pd of the L1 model decrease when the background radiometry increases, which is consistent with the non-uniformity of detected scatterers observed in image 7b.

#### V. AN APPLICATION TO CHANGE DETECTION

##### A. Method

In this section, we propose a direct application of our decomposition model for change detection, under the hypothesis that changes mostly affect the scatterers. This assumption is likely to be fulfilled in urban or industrial areas.

Given a time-series  $\mathbf{v}$ , the model described in section II-C provides multi-temporal decomposition  $\{(\mathbf{u}_{B1}, \mathbf{u}_{S1}, \dots, \mathbf{u}_{Bn}, \mathbf{u}_{Sn})\}$ , or in the case of a time-invariant background

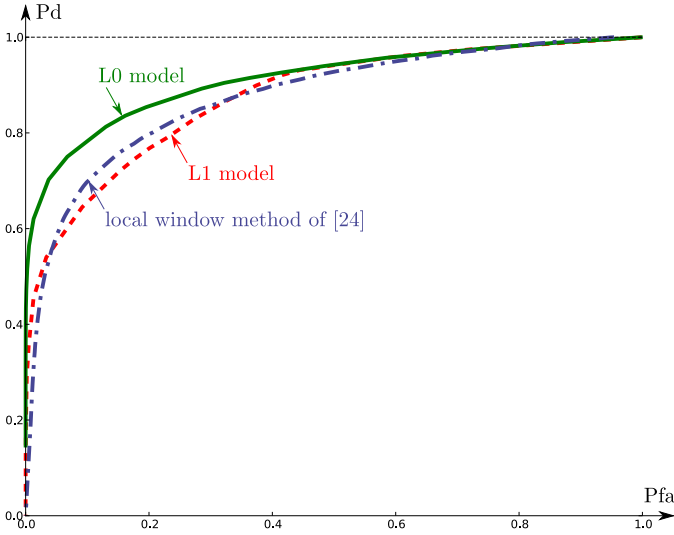
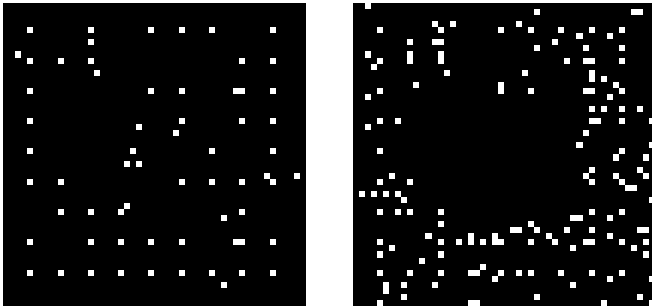


Fig. 6. Receiver operating curve (ROC) between L0 and L1 version of our model and a method based on local window analysis [24].



(a) Scatterers image obtained using the proposed decomposition (with L0 term),  $\lambda = 2.5$  (b) Scatterers image obtained using L1 version,  $\lambda = 0.012$

Fig. 7. 2 images of scatterers achieving the same probability of detection: left with an L0 penalty, right with an L1 penalty.

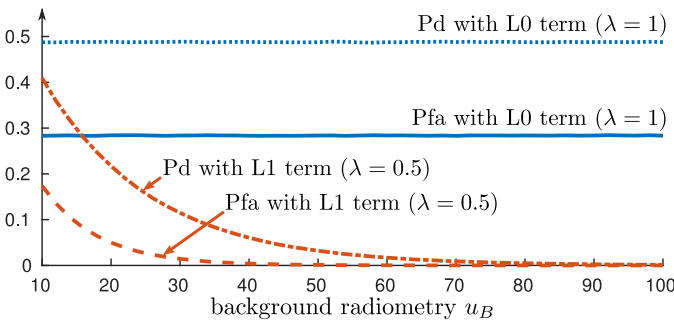


Fig. 8. With an L1 penalty, the probability of false alarm Pfa and the probability of detection Pd vary with the background radiometry.

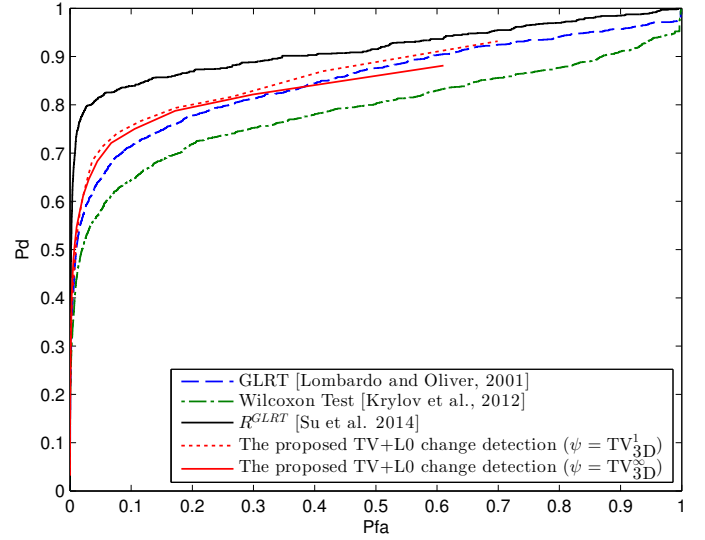


Fig. 9. ROC curve of various change detection algorithms

( $\psi = \text{TV}_{3\text{D}}^\infty$  in equation 6):  $\{(\mathbf{u}_B, \mathbf{u}_{S_1}), \dots, (\mathbf{u}_B, \mathbf{u}_{S_n})\}$ . Change detection cannot be performed directly by pixel differences on the images of scatterers because the location and radiometry of scatterers fluctuate from one image to another even when insignificant changes happen in the scene. We therefore first threshold the scatterers images  $\{\mathbf{u}_{S_t}\}$  (noted in the following  $\{\mathbf{u}_{S_t}^{\text{bin}}\}$ ) to make the method insensitive to radiometric fluctuations. Robustness to small changes in the detected location of a scatterer is obtained by considering spatial neighborhoods:

$$C_{t,t'}(i) = \left| \sum_{\delta} \mathbf{u}_{S_t}^{\text{bin}}(i + \delta) - \sum_{\delta} \mathbf{u}_{S_{t'}}^{\text{bin}}(i + \delta) \right| \quad (22)$$

where  $\mathbf{u}_{S_t}$  and  $\mathbf{u}_{S_{t'}}$  are the two images extracted from the decomposition of the time series,  $\delta$  is a shift to iterate over the neighborhood of the pixel  $i$  so  $C_{t,t'}(i)$  is the difference between the number of scatterers present in the window centered in  $i$  in one image and the number of scatterers in the other one. This map is then thresholded to locate the changes between the two images.

## B. Results

To illustrate the results of our method, we ran this algorithm on a SAR time series from Saint-Gervais (France) acquired by TerraSAR-X satellite. This time series is composed of 26 single-look images. 13 of these images have been sensed in 2009, 13 in 2011. The ground-truth used for the quantitative results have been labeled manually by [37]. We compare the results of this algorithm with other change detection methods in figure 9 and show an example of detected changes in figure 10. The ROC curve is obtained by varying the threshold applied on  $C_{t,t'}$ . Since all changes do not occur as scatterers changes, the ROC curves with our method do not reach high levels of probability of detection Pd. This simple thresholding approach achieves a performance comparable or superior to the methods described in [38] and [39]. Change



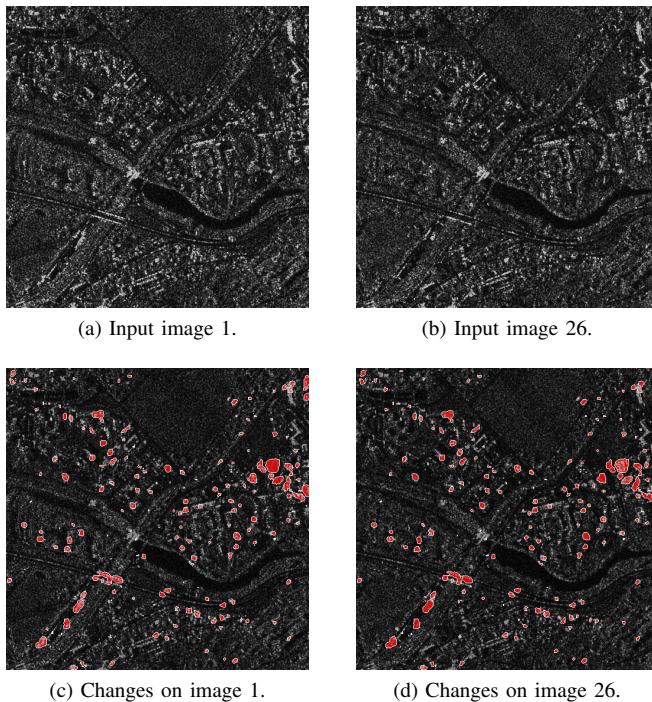


Fig. 10. Change detection results using the proposed method on images of Saint-Gervais series. Regions with changes that have been detected are circled in white.

detection based solely on the detected scatterers however is less accurate than the recent work by Su *et al.* [37]. Note that the simpler decomposition with a time-invariant background ( $\psi = \text{TV}_{3\text{D}}^\infty$ ) gives worse detection results. A reason for this worse performance may come from the degradation of the detection of scatterers when the background is not correctly estimated, as is the case of regions where the background undergoes some changes.

## VI. CONCLUSION

This paper establishes the connection between a formulation of scatterers detection based on detection theory and the maximum *a posteriori* estimation with L0 pseudo-norm regularization. The problem of jointly detecting scatterers and estimating the background radiometry is then expressed as an image decomposition, stated as a combinatorial minimization problem. To solve this challenging large-scale combinatorial minimization problem, we propose to compute the minimum-cut of a 4-D graph. Application to large areas and time series with numerous dates requires a limited memory algorithm based on block-processing with overlap. The comparison of the proposed L0-based decomposition with an L1-based decomposition shows a clear advantage for our formulation, which justifies tackling the combinatorial optimization problem. Our formulation gives constant false alarm rate and constant correct detection rate when the background level varies, in contrast to the L1 model. Finally, a simple application of the spatio-temporal decomposition is shown in the context of change detection.

Other decomposition models may be considered in the future, provided that they fulfill the constraints required to

apply the graph-cut optimization method. Future work includes considering models designed for change detection rather than resorting to a post-processing step. The optimization step could be modified to use recent algorithms for min-cut computation (see [32], [33]). The fusion approach proposed in [40] could also be adapted to include information from an optical image in the computation of the multi-temporal background component.

## ACKNOWLEDGMENT

The authors would like to thank the German Aerospace Agency (DLR) for the images (projects MTH0232 and LAN1746). This work has been funded by the CNES and the “Future et Ruptures” (Institut Mines-Télécom) program.

## REFERENCES

- [1] J. Lee, S. Cloude, K. Papathanassiou, M. Grunes, and I. Woodhouse, “Speckle filtering and coherence estimation of polarimetric SAR interferometry data for forest applications,” *IEEE Trans. Geosci. Remote Sens.*, vol. 41, no. 10, 2003.
- [2] G. Vasile, E. Trouvé, and J. Lee, “Intensity-Driven Adaptive-Neighborhood Technique for Polarimetric and Interferometric SAR Parameters Estimation,” *IEEE Trans. Geosci. Remote Sens.*, vol. 44, no. 6, 2006.
- [3] A. Buades, B. Coll, and J.-M. Morel, “A review of image denoising algorithms, with a new one,” *Multiscale Modeling & Simulation*, vol. 4, no. 2, pp. 490–530, 2005.
- [4] C.-A. Deledalle, L. Denis, and F. Tupin, “Iterative weighted maximum likelihood denoising with probabilistic patch-based weights,” *IEEE Trans. Image Process.*, vol. 18, no. 12, pp. 2661–2672, 2009.
- [5] —, “NL-InSAR: Nonlocal interferogram estimation,” *IEEE Trans. Geosci. Remote Sens.*, vol. 49, no. 4, pp. 1441–1452, 2011.
- [6] J. Chen, Y. Chen, W. An, Y. Cui, and J. Yang, “Nonlocal filtering for polarimetric SAR data: A pretest approach,” *IEEE Trans. Geosci. Remote Sens.*, vol. 49, no. 5, 2011.
- [7] H. Zhong, Y. Li, and L. Jiao, “SAR Image Despeckling Using Bayesian Nonlocal Means Filter With Sigma Preselection,” *IEEE Geosci. Remote Sens. Lett.*, vol. 8, no. 4, 2011.
- [8] S. Parrilli, M. Poderico, C. Angelino, and L. Verdoliva, “A Nonlocal SAR Image Denoising Algorithm Based on LLMMSE Wavelet Shrinkage,” *IEEE Trans. Geosci. Remote Sens.*, vol. 50, no. 2, 2012.
- [9] D. Cozzolino, S. Parrilli, G. Scarpa, G. Poggi, and L. Verdoliva, “Fast adaptive nonlocal sar despeckling,” *Geoscience and Remote Sensing Letters, IEEE*, vol. 11, no. 2, pp. 524–528, Feb 2014.
- [10] C.-A. Deledalle, L. Denis, F. Tupin, A. Reigber, and M. Jäger, “Nl-sar: A unified nonlocal framework for resolution-preserving (pol)(in)sar denoising,” *Geoscience and Remote Sensing, IEEE Transactions on*, vol. 53, no. 4, pp. 2021–2038, April 2015.
- [11] A. Achim, P. Tsakalides, and A. Bezerianos, “SAR image denoising via Bayesian wavelet shrinkage based on heavy-tailed modeling,” *IEEE Trans. Geosci. Remote Sens.*, vol. 41, no. 8, 2003.
- [12] F. Argenti, T. Bianchi, and L. Alparone, “Multiresolution MAP Despeckling of SAR Images Based on Locally Adaptive Generalized Gaussian pdf Modeling,” *IEEE Trans. Image Process.*, vol. 15, no. 11, pp. 3385–3399, 2006.
- [13] H. Xie, L. Pierce, and F. Ulaby, “SAR speckle reduction using wavelet denoising and Markov random field modeling,” *IEEE Trans. Geosci. Remote Sens.*, vol. 40, no. 10, pp. 2196–2212, Jan. 2002.
- [14] L. I. Rudin, S. Osher, and E. Fatemi, “Nonlinear total variation based noise removal algorithms,” *Physica D: Nonlinear Phenomena*, vol. 60, no. 1, pp. 259–268, 1992.
- [15] J.-F. Aujol, G. Aubert, L. Blanc-Féraud, and A. Chambolle, “Image decomposition application to sar images,” in *Scale Space Methods in Computer Vision*. Springer, 2003, pp. 297–312.
- [16] L. Denis, F. Tupin, J. Darbon, and M. Sigelle, “Sar image regularization with fast approximate discrete minimization,” *Image Processing, IEEE Transactions on*, vol. 18, no. 7, pp. 1588–1600, 2009.
- [17] F. Palsson, J. R. Sveinsson, M. Ulfarsson, and J. A. Benediktsson, “SAR image denoising using total variation based regularization with SURE-based optimization of the regularization parameter,” in *Geoscience and Remote Sensing Symposium (IGARSS), 2012 IEEE International*, July 2012, pp. 2160–2163.



- [18] G. Aubert and J.-F. Aujol, "A variational approach to removing multiplicative noise," *SIAM Journal on Applied Mathematics*, vol. 68, no. 4, pp. 925–946, 2008.
- [19] G. Steidl and T. Teuber, "Removing multiplicative noise by douglas-rachford splitting methods," *Journal of Mathematical Imaging and Vision*, vol. 36, no. 2, pp. 168–184, 2010.
- [20] J. M. Bioucas-Dias and M. A. Figueiredo, "Multiplicative noise removal using variable splitting and constrained optimization," *Image Processing, IEEE Transactions on*, vol. 19, no. 7, pp. 1720–1730, 2010.
- [21] F. Argenti, A. Lapini, T. Bianchi, and L. Alparone, "A tutorial on speckle reduction in synthetic aperture radar images," *Geoscience and Remote Sensing Magazine, IEEE*, vol. 1, no. 3, pp. 6–35, 2013.
- [22] C.-A. Deledalle, L. Denis, G. Poggi, F. Tupin, and L. Verdoliva, "Exploiting Patch Similarity for SAR Image Processing: The nonlocal paradigm," *Signal Processing Magazine, IEEE*, vol. 31, no. 4, pp. 69–78, July 2014.
- [23] A. Lopes, E. Nezry, Goze, R. Touzi, and A. Solaas, "Adaptive processing of multilook complex SAR images," in *Geoscience and Remote Sensing Symposium, 1992. IGARSS '92. International*, vol. 2, May 1992, pp. 890–892.
- [24] A. Lopes, E. Nezry, R. Touzi, and H. Laur, "Structure detection and statistical adaptive speckle filtering in SAR images," *International Journal of Remote Sensing*, vol. 14, no. 9, pp. 1735–1758, 1993.
- [25] L. Denis, F. Tupin, and X. Rondeau, "Exact discrete minimization for TV+L0 image decomposition models," in *Image Processing (ICIP), 2010 17th IEEE International Conference on*. IEEE, 2010, pp. 2525–2528.
- [26] S. Lobry, L. Denis, and F. Tupin, "Sparse & smooth decomposition models for multi-temporal SAR images," in *Analysis of Multitemporal Remote Sensing Images (Multi-Temp), 2015 8th International Workshop on the*, July 2015, pp. 1–4.
- [27] S. Kay, "Fundamentals of statistical signal processing, Vol. II: Detection Theory," *Prentice Hall*, 1998.
- [28] H. Ishikawa, "Exact optimization for Markov random fields with convex priors," *Pattern Analysis and Machine Intelligence, IEEE Transactions on*, vol. 25, no. 10, pp. 1333–1336, 2003.
- [29] Y. Boykov and V. Kolmogorov, "Computing geodesics and minimal surfaces via graph cuts," in *Computer Vision, 2003. Proceedings. Ninth IEEE International Conference on*. IEEE, 2003, pp. 26–33.
- [30] J. W. Goodman, *Speckle phenomena in optics: theory and applications*. Roberts and Company Publishers, 2007.
- [31] Y. Boykov and V. Kolmogorov, "An experimental comparison of min-cut/max-flow algorithms for energy minimization in vision," *Pattern Analysis and Machine Intelligence, IEEE Transactions on*, vol. 26, no. 9, pp. 1124–1137, 2004.
- [32] J. Liu and J. Sun, "Parallel graph-cuts by adaptive bottom-up merging," in *Computer Vision and Pattern Recognition (CVPR), 2010 IEEE Conference on*, June 2010, pp. 2181–2188.
- [33] O. Jamriska, D. Sykora, and A. Hornung, "Cache-efficient graph cuts on structured grids," in *Computer Vision and Pattern Recognition (CVPR), 2012 IEEE Conference on*, June 2012, pp. 3673–3680.
- [34] L. Denis, F. Tupin, J. Darbon, and M. Sigelle, "SAR image regularization with fast approximate discrete minimization," *Image Processing, IEEE Transactions on*, vol. 18, no. 7, pp. 1588–1600, July 2009.
- [35] A. Shabou, J. Darbon, and F. Tupin, "A markovian approach for insar phase reconstruction with mixed discrete and continuous optimization," *Geoscience and Remote Sensing Letters, IEEE*, vol. 8, no. 3, pp. 527–531, May 2011.
- [36] J. Tropp *et al.*, "Just relax: Convex programming methods for identifying sparse signals in noise," *Information Theory, IEEE Transactions on*, vol. 52, no. 3, pp. 1030–1051, 2006.
- [37] X. Su, C.-A. Deledalle, F. Tupin, and H. Sun, "NORCAMA: Change Analysis in SAR Time Series by Likelihood Ratio Change Matrix Clustering," *ISPRS Journal of Photogrammetry and Remote Sensing*, pp. 247–261, May 2014.
- [38] P. Lombardo and C. Oliver, "Maximum likelihood approach to the detection of changes between multitemporal SAR images," *IEEE Proceedings-Radar, Sonar and Navigation*, vol. 148, no. 4, pp. 200–210, 2001.
- [39] V. Krylov, G. Moser, A. Voisin, B. Serpico, Sebastiano, and J. Zerubia, "Change detection with Synthetic Aperture Radar images by Wilcoxon statistic likelihood ratio test," in *IEEE International Conference on Image Processing 2012*, Orlando, United States, Sep 2012.
- [40] L. Denis, F. Tupin, J. Darbon, and M. Sigelle, "Joint regularization of phase and amplitude of insar data: Application to 3-D reconstruction," *Geoscience and Remote Sensing, IEEE Transactions on*, vol. 47, no. 11, pp. 3774–3785, Nov 2009.